Geometric feedback control of discrete-deposition SFF systems

Daniel L. Cohen
Department of Mechanical Engineering, Cornell University, Ithaca, New York, USA, and

Hod Lipson
Department of Mechanical Engineering, Cornell University, Ithaca, New York, USA and
Department of Computing & Information Science, Cornell University, Ithaca, New York, USA

Abstract

Purpose – New applications of solid freeform fabrication (SFF) are arising, such as functional rapid prototyping and *in situ* fabrication, which push SFF to its limits in terms of geometrical fidelity due to the applications' inherent process uncertainties. Current closed-loop feedback control schemes monitor and manipulate SFF techniques at the process level, e.g. envelope temperature, feed rate. "Closing the loop" on the process level, instead of the overall part geometry level, leads to limitations in the types of errors that can be detected and corrected. The purpose of this paper is to propose a technique called greedy geometric feedback (GGF) control which "closes the loop" on the overall part geometry level.

Design/methodology/approach – The overall part geometry is monitored throughout the print and, using a greedy algorithm, real-time decisions are made to serially determine the locations of subsequent droplets, i.e. overall part geometry is directly manipulated. A computer simulator and a physical experimental platform were developed to compare the performance of GGF to an open-loop control scheme. Root mean square surface height errors were measured under controlled uncertainties in droplet height, droplet radius of curvature, droplet positioning and mid-print part deformations.

Findings – The GGF technique outperformed open-loop control under process uncertainties in droplet shape, droplet placement and mid-print part deformations. The disparity between performances is dependant on the nature and extent of the imposed process uncertainties.

Practical implications – Future research will focus on improving the performance of GGF for specific cases by designing more complex greedy algorithmic scoring heuristics. Also, the technique will be generalized beyond heightmap representations of 3D spaces.

Originality/value – The GGF technique is the first to "close the loop" on the overall part geometry level. GGF, therefore, can compensate for a broader range of errors than existing closed-loop feedback control schemes. Also, since the technique only requires the real-time update of a very limited set of heights, the technique is computationally inexpensive and widely applicable. By developing a closed-loop feedback scheme that addressed part geometry-level errors, SFF can be applied to more challenging *in situ* fabrication scenarios with less conventional materials.

Keywords Feedback, Control systems, Geometry, Uncertainty management, Discrete control systems

Paper type Research paper

1. Introduction

Solid freeform fabrication (SFF) is evolving to address new applications, such as *in situ* manufacture (Bodiford *et al.*, 2005) and the fabrication of fully functional components (Lipson, 2005). Along with these innovative applications come the technological challenges associated with a variety of process uncertainties, including "situational," "environmental," and "build-material" uncertainties (Figure 1). Existing control schemes attempt to harness closed-loop feedback control in order to achieve desirable geometric fidelity in the face of some process uncertainties (Mallikharjuna *et al.*, 2001). However, these specific control schemes are limited in the types of uncertainties for which they can correct. Moreover, they are susceptible to changes or inaccuracies in the models that relate whole-part geometry to low-level process variables.

In this paper, we propose a closed-loop feedback control scheme, which we call greedy geometric feedback (GGF) control. Unlike other schemes which indirectly control part geometry by monitoring and manipulating low-level system parameters (e.g. build-material flow rate, temperature, head position), GGF directly monitors whole-part geometry and directly manipulates the location of deposited matter to compensate for geometric inaccuracies. We suggest that "closing the loop" at the whole-part geometry level, rather than

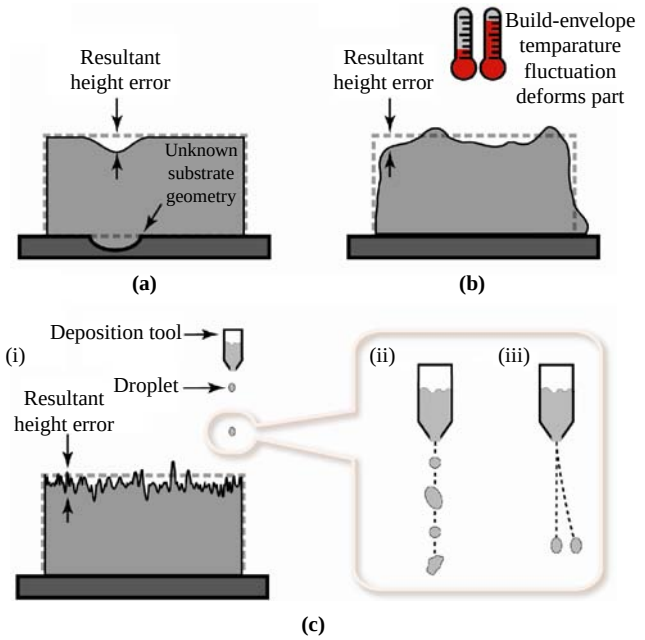
The current issue and full text archive of this journal is available at **www.emeraldinsight.com/1355-2546.htm**

Rapid Prototyping Journal
16/5 (2010) 377–393
© Emerald Group Publishing Limited [ISSN 1355-2546]
[DOI 10.1108/13552541011065777]

This research is performed under appointments to the Department of Homeland Security Fellowship Program and the National Science Foundation Graduate Research Fellowship Program #DGE0202748.

Received: 4 December 2007
Revised: 6 March 2009, 14 May 2009
Accepted: 19 May 2009

Figure 1 Three classes of process uncertainties relevant to printing



Notes: Cross-sections of printed parts (box-shaped dotted outlines signify intended geometries and shaded solid outlines represent actual printed objects); (a) an example of "situational uncertainty" in which an unknown substrate geometry causes a geometric defect in the printed part and results in a height error; (b) an example of "environmental uncertainty" in which build-envelope temperature fluctuation causes deformation via melting and results in height errors; (c) – (i) An example of "build-material uncertainty" in which unstable material properties lead; (ii) varying droplet size/shape; (iii) varying droplet positioning, causing geometric defects and resulting in height errors

at the process-variable level, increases the extent to which process uncertainties can be detected and corrected, and thus allows for the compensation of a wider range of process uncertainties. We also suggest that this technique is more generalized in that it does not rely upon the knowledge of any specific relationships between whole-part geometry and low-level process variables.

2. Problem statement

New applications of SFF, such as *in situ* manufacture (Cooper *et al.*, 2004) and the fabrication of fully functional components (Malone and Lipson, 2004), have inherent process uncertainties that can potentially diminish the geometric fidelity of the fabricated parts. Three classes of process uncertainties are especially relevant: "situational," "environmental," and "build-material" uncertainties.

An application that exemplifies both "situational" and "environmental" process uncertainties is *in situ* SFF. In the literature, the term "*in situ* SFF" refers to layered manufacturing (LM) where the fabrication substrate has a complex or arbitrary geometry. For example, *in situ* SFF could refer to LM on top of a pre-existing part (Whitney, 2004) or the use of LM to embed one component within another (Sun *et al.*, 1998). The uncertainty in substrate geometry during *in situ* prints is one example of situational process uncertainty Figure 1(a).

Furthermore, if the pre-existing target substrate [e.g. external armor of a battle tank (Pérès and Noyes, 2006) or internal cavity of a human body (Cohen *et al.*, 2006)] is unable to be placed within a traditional SFF machine (e.g. due to large substrate size or sterility), then the SFF system must be capable of operating within the substrate's environment. While operating within the substrate's environment, the SFF system faces a less certain process parameter landscape, i.e. the SFF system is subject to substantial environmental process uncertainty. *In situ* environmental conditions such as vibration, substrate movement, humidity variation, temperature fluctuation and substrate-on-part squeeze, are factors that could pose environmental process uncertainties and result in diminished geometric fidelity of the part Figure 1(b).

In addition to situational and environmental process uncertainties, a third class of process uncertainty is "build-material uncertainty." An application of SFF that demonstrates materials-based process uncertainty is the LM of fully functional components. While some functional components can be rapid prototyped with reasonable parametric certainty under open-loop control (Vaidyanathan, 2000), other techniques face greater process uncertainty. Laser metal deposition (LMD) is an SFF technique with inherent process uncertainty that is used for producing functional metal components (Mallikharjuna *et al.*, 2001). Also, syringe extrusion-based approaches to LM of fully functional electro-mechanical components are fraught with process uncertainty due to its materials' non-homogeneity, unfavorable viscosities and viscoelasticity (Malone *et al.*, 2004). Additionally, the hydrogels used in fabricating living, functional biological constructs are also particularly challenging to print (Federovich *et al.*, 2007). This is due to materials-based phenomena such as background polymer cross-linking reactions, phase separation, non-homogenous composition, low strength and viscoelastic behavior (Cohen *et al.*, 2006). These non-traditional, functional SFF materials behave unpredictably and cause the fabricated components to have diminished geometric fidelity Figure 1(c).

While there are several classes of process uncertainties, and numerous examples of each, they will manifest themselves either at the process-variable level, e.g. droplet shape/position errors Figure 1(c) or at the whole-part geometry level, e.g. during-print part-shape deformations Figure 1(b). Ultimately, the result of these process uncertainties is some height error between the intended and the actual part geometries (Figure 1).

Open-loop control schemes are insufficient for some of the more innovative applications of SFF (Taminger *et al.*, 2002). More advanced control schemes must be developed to achieve a desirable geometric fidelity despite under-constrained printing circumstances and/or inherently uncertain SFF processes and materials.

3. Prior work

Low-level closed-loop feedback control schemes have been implemented in many SFF systems to improve the geometric fidelities of printed parts. However, none of the approaches directly monitored the whole-part geometry. Instead, they monitored and manipulated low-level system variables such as machine temperature, material feedrate and individual droplet shape, anticipating that this would lead to better part geometry.

Rapid Prototyping Journal
Volume 16 · Number 5 · 2010 · 377–393

Low-level, independent SFF process variables are commonly stabilized in both research and commercial rapid prototyping (RP) systems using closed-loop feedback control. Process variables such as substrate position, envelope temperature, deposition tool temperature, laser power and material feedrate are often stabilized using closed-loop feedback control (Hu *et al.*, 2002). In these cases, a low-level independent variable is monitored and directly actuated. For example, the envelope temperature is directly monitored with a temperature sensor and then directly manipulated with a heating element. However, these low-level independent process variables have only an indirect influence on the final part geometry.

On a slightly higher level, dependent process variables have also been stabilized. For example, in LMD systems, melt pool depth was stabilized with a proportional-integral-derivative controller by monitoring the melt pool profile, inferring the melt pool depth and then manipulating laser power and traverse speed (Derouet *et al.*, 1997). However, these examples of dependent variable regulation are still low-level control schemes because whole-part geometry itself is not being directly monitored/manipulated; there is an indirect relationship between these dependent process variables and the whole-part geometry.

On yet a higher level of control, droplet geometry has been stabilized through closed-loop control. Geometric profiles of deposited beads were used to regulate the bead height through the manipulation of laser power (Mazumder *et al.*, 1999). Distributed-parameter modeling was used to generate real-time surface geometry models by identifying droplets' geometric parameters during-print (Doumanidis and Skordeli, 2000). This distributed-parameter model was used in conjunction with a PI-controller to regulate bead geometry through the manipulation of traverse speed and material feed rate (Doumanidis and Kwak, 2001). Closed-loop feedback control has also been applied to non-LMD SFF systems. For example, computer vision feedback was used to regulate droplet diameter by manipulating the differential pressure of continuous mode materials-jetting systems (Lovelady and Watts, 1999). However, these control schemes are still low-level approaches because whole-part geometry is not directly monitored/manipulated; there is an indirect relationship between the droplet shape and final overall shape of the part.

Since none of these aforementioned closed-loop feedback schemes "close the loop" at the level of whole-part geometry, none of them can account for errors that occur at a higher level than the process-variable level. Even monitoring the shapes of individual droplets leaves room for higher level errors (i.e. errors occurring in the whole-part geometry) to be undetectable. Furthermore, none of the prior control techniques directly manipulates the shape of the overall geometry and consequently they have potentially limited ability to correct for errors that occur on the whole-part geometry level (such as during-print whole-part deformation, as well as an uneven substrate). In addition to the notion that the existing control schemes mentioned, are limited in the extent to which process uncertainties can be observed and corrected, the disconnect between low-level process variables and the whole-part geometry causes existing feedback control schemes to be vulnerable to changes in the relationships between process variables and whole-part geometry. Existing control schemes are often critically reliant upon models of the relationships between low-level process variables and whole-part geometry, yet these relationships are susceptible to change.

4. Proposed concept: GGF control

4.1 Overview of two embodiments of GGF scheme

The general concept behind the proposed GGF control scheme is that the system iteratively decides where to place droplets at run-time based on geometric feedback. During each iteration, using geometric measurements and a model of the target object, the system chooses appropriate locations for subsequent droplets such that the fabricated part ultimately matches the target geometry. The system chooses these deposition locations from a set of candidate locations by selecting those candidates with the highest scores, as defined by a user-selected heuristic. Since the system chooses the best candidates during each iteration, the algorithm is considered to be "greedy". This greedy algorithmic process replaces the more traditional path planning performed a priori by most SFF systems.

There are two embodiments of the GGF control scheme proposed herein. The first embodiment, local-GGF considers a limited number of candidate locations during each iteration. In other words, the algorithm iteratively decides where to place the subsequent droplet by searching a local selection space, i.e. a set of locations immediately surrounding the previously deposited droplet.

The second embodiment of the GGF control scheme is global-GGF. In this embodiment, during each iteration, the algorithm chooses one or more locations for subsequent droplets from the global selection space, i.e. the set of all possible deposition locations throughout the entire build envelope.

Whereas local-GGF only requires a limited set of geometric measurements (e.g. heights at 4, 6 or 8 locations immediately surrounding the previously deposited droplet) to be performed during each iteration, global-GGF requires a global scan during each iteration. The global scans required by global-GGF are more expensive than the local scans required by local-GGF. However, countering this increased expense of scanning, global-GGF selects a plurality of droplet locations per iteration whereas local-GGF only selects one droplet location per iteration.

The commonality between both embodiments, and the crux of the GGF scheme proposed in this paper, is that both variants at run-time iteratively choose deposition locations with the highest scores from their respective selection spaces.

4.2 Local-GGF

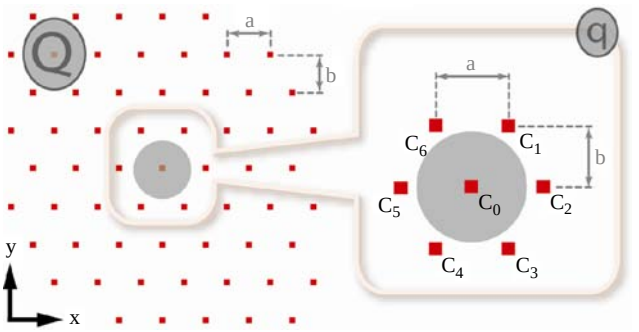
4.2.1 First iteration of algorithm

The iterative decision making process begins with the deposition of a seed droplet at a random location within the "global selection space," Q Figure 2(a). The global selection space is the set of all possible locations of subsequent droplets. Since droplets can only be placed at fixed intervals, this space is discrete.

However, scanning the entire global selection space after the placement of each droplet is both computationally expensive and time consuming. Therefore, it is more efficient to iteratively perform updates on only a small subset of the global selection space after each droplet is placed and then to use this subset as the selection space for the decision of where to place the subsequent droplet.

This subset of the global selection space is referred to as the "local selection space," q Figure 2(b). The local selection space is the set of seven positions that includes the location of the previously deposited droplet (i.e. the current position of the deposition tool) plus its six neighbors.

Figure 2 Diagram of selection spaces



Notes: (a) Global selection space, Q, in which the circle represents a droplet and the squares represent candidate locations of subsequent droplets; (b) local selection space, q, with seven candidate locations, C_0 through C_6, and the vertical and horizontal spacing intervals, b and a, respectively

Each position within the local selection space, q, is considered to be a candidate for the placement of the subsequent droplet and the system measures the heights at each candidate location. These seven candidate locations, C_i, are assigned scores based upon a particular scoring heuristic. While this heuristic can be designed with more complexity, we shall choose this heuristic simply to be the difference between the intended and actual heights at a particular (x,y) coordinate for the purposes of this paper. This score is essentially the real-time height error of a certain position:

$$S(x,y,t) = T(x,y) - A(x,y,t) \quad (1)$$

where $S(x,y,t)$ is the score, $T(x,y)$ is the height of the intended target geometry and $A(x,y,t)$ is the height of the build surface.

Once heuristic scores are assigned to all seven candidates within the local selection space, the candidate with the highest score becomes the location of the next droplet. If more than one candidate share the value of the maximum heuristic score, then the algorithm randomly selects among them as long as C_0 is not one of the tied candidates. If C_0 is one of the candidates that happen to share the value of the maximum score, then C_0 is given priority and is selected. This last rule serves to reduce the number of tool movements.

4.2.2 Main loop: iterative decision making

The process of measuring local selection space heights and then selecting a location for the next droplet is repeated. As long as one of the candidates within the local selection space has a score above some threshold, L, the iterative cycle continues.

The threshold, L, can be user-selected depending on the specific scoring heuristic used. In this case, with the scoring heuristic being the real-time height error, the threshold, L, is simply zero. That is, the print continues as long as at least one of the candidates has a positive height error.

A deadlock is temporarily reached when none of the candidates within the local selection space has a score above the threshold. At this point, the system has satisfied the "halt condition" and it breaks the iterative cycle to address the circumstance.

4.2.3 Halt and end conditions

The iterative decision making (and hence the printing process) halts when none of the candidates in the local selection space is viable, i.e. none of the candidate scores is greater than the score threshold:

$$\text{Halt condition} : S(q) \leq L \quad (2)$$

When the halt condition is satisfied, the algorithm searches for a "reinsertion point", i.e. a position within the global selection space at which the candidate score is viable. The re-insertion point may be found through a random walk or brute force search (i.e. complete scan of global selection space). In the simulations and physical experiments conducted for this paper, reinsertion points were found through brute force searches by selecting the point in the global decision space with the highest heuristic score. If a viable reinsertion point is found, then the iterative decision making process continues, starting at this point. If no viable reinsertion point is found, then the "end condition" is satisfied and the print is finished:

$$\text{End condition} : S(Q) \leq L \quad (3a)$$

4.3 Global-GGF

4.3.1 Main loop: iterative decision making

During each iteration of the global-GGF algorithm, a scan of the global selection space is conducted. Each candidate position within the global selection space is assigned a score, in a fashion similar to the scoring process of local-GGF.

After each scan, the top H candidates within the global selection space are chosen to become the locations of the next set of droplets, where H is the maximum number of locations at which droplets can be placed during a single iteration, i.e. per scan of the global selection space.

4.3.2 End condition

The iterative process ends when none of the candidates within the global selection space has a score above some threshold, L. As in Local-GGF, L is user selected and for the purposes of this paper taken to be zero. That is, with the scoring heuristic being the real-time height error and the threshold being zero, the print ends when none of the locations within the global selection space has a positive height error:

$$\text{End condition} : S(Q) \leq L \quad (3b)$$

4.4 Practical considerations

4.4.1 Alternative configurations of the selection space

In the experimentation conducted herein, we primarily considered the particular implementation of GGF in which droplets were hexagonally packed. That is, the global selection space was a large set of hexagonally packed points and the local selection space comprised the location of the previously deposited droplet and its six, six-connected neighbors (six-connectivity). However, a hexagonally packed selection space is not the only conceivable configuration. A square lattice packing of droplets could also be considered; within the square lattice packing configuration, the local selection space could either be based upon four- or eight-connectivity. That is, with a square lattice packing of droplets, the local selection space could either be the previously deposited droplet's location and its four, four-connected neighbors or it could be the previously deposited droplet's location and its eight, eight-connected neighbors.

We only implemented the six-connectivity configuration in our physical experiments. While we primarily focused on hexagonal

packing, this configuration is not necessarily the optimal choice for either efficiency or effectiveness. The selection of the optimal configuration would depend on time requirements, metrology constraints, droplet packing behavior, as well as the specific efficiency/accuracy tradeoff landscape. The optimality of the selection space configuration is beyond the scope of this proof-of-concept treatment of the GGF algorithm.

4.4.2 Metrology/height measurement

GGF is independent of the specific imaging modality used for collecting the necessary height information during the print. The computational simulations make no reference to any specific imaging modality, as height information is all that is required by the GGF algorithm. For the physical experimentation, we chose the Microtrak II complementary metal oxide semiconductor (CMOS). laser triangulation distance sensor (MTI Instruments Inc., Albany, NY, USA). Again, numerous other imaging modalities could also conceivably be used including camera-based computer vision techniques, or for *in situ* medical applications, real-time computed tomography.

Furthermore, in our particular implementation with the Microtrak II laser sensor we are only able to measure one point at a time. For Local-GGF, in order to scan the local selection space, the gantry robot had to move the sensor to each position sequentially. However, future advancements in metrology could conceivably enable the real-time monitoring of the entire local selection space. For example, arrays of point sensors or line scanners could be mounted in near proximity to the deposition tool to enable real-time geometric data acquisition.

While future advancements could enable real-time measurement of local selection spaces for Local-GGF, currently available metrology technology can make scanning the global selection space substantially more efficient (which would benefit Global-GGF as well as the re-insertion point searches of Local-GGF). Commercially available laser line scanners, such as the M2D scanner (Mikroelektronik GmbH, Munich, Germany) could capture the entire global selection space with a single swipe across the build part. Single swipes across the build surface are relatively low cost. Moreover, considering that some commercial RP systems such as the Eden Series (Objet Geometries Inc., Billerica, MA, USA) already require the printhead to swipe across the entire build part for each layer, adding a laser line scanner to such RP systems could enable seamless geometric data acquisition.

4.4.3 Deposition technology

The discretized, serial decision making of GGF naturally lends itself to suitability for drop-on-demand RP systems. The computational simulations were based upon drop-on-demand deposition and our physical implementation used a custom wax droplet deposition tool. However, the GGF algorithm is directly applicable to any deposition technology in which the material deposition is discretized.

Continuous filament-based deposition techniques are conceivably relevant if the deposition were discretized into "virtual packets" of material. However, it should be noted that depositing small volumes in a continuous filament system is quite challenging as they tend to excel in long-path printing situations. It remains to be seen, in future experimentation, to what extent the GGF algorithm is feasible for such continuous filament deposition systems.

4.4.4 Multi-nozzle implementation and parallelization

Within the drop-on-demand regime, this algorithm is not limited to single nozzle deposition; commercially available deposition heads comprising an array of hundreds of nozzles can be used with GGF. With an array of hundreds of nozzles, multiple nozzles may be fired simultaneously forming droplet primitives that range in size from that produced by one nozzle to any number of nozzles, i.e. "super-primitives" may be formed of arbitrary size and shape. The choice of primitive size and shape, in the case of an array-based deposition head, would be selected depending on the resolution/print speed trade-off landscape and the operator's specific needs.

Another consideration relating to boosting the speed of GGF prints is the notion of parallelization. While Global-GGF inherently deposits a plurality of droplets per iteration, Local-GGF deposits one droplet per iteration. However, the localized nature of Local-GGF can be exploited by having multiple deposition heads operate on different regions of the part.

4.4.5 Droplet scale and print resolution

It is important to note that GGF is dimensionless in that it is conceptually valid at any scale of droplet or part size. While specific scales were selected for simulation and physical implementation, these scales are only representative of this approach's capability. GGF could be implemented on smaller scale systems than those studied herein. At the extreme end of the size scale, metrology considerations become increasingly important, however these challenges stand to be overcome by future metrology advancements, as the GGF algorithm itself is conceptually valid at any scale.

4.4.6 Determination of operating parameters

While this approach notably does not demand detailed modeling of the underlying process physics, as it operates on a high (whole-part) level, certain parameters must still be selected. These operating parameters include primarily, a and b, the vertical and horizontal spacing intervals between droplets. In the experimentation performed herein, these parameters were selected based on which combination gave the smoothest surface packing for a specific nominal droplet geometry. However, further investigation could unveil a better method for selecting operating parameters, including a computational learning approach (e.g. genetic algorithms) in which the parameters are efficiently and automatically optimized over a wide range of values.

As for selection of the threshold, L, in simulation this parameter was tuned to achieve optimal results. However, in practice, it was found to be an unimportant parameter to tune. Simply setting the parameter equal to 0 produced indistinguishable from other tunings since the physical noise had a much more profound impact on the print. Furthermore, the worst case with an improper tuning is that an additional layer is deposited; the deposition of a single, additional layer is a nuance too small to carry much import in a realistic implementation.

5. Computational simulator for GGF

5.1 Overview

We developed a Matlab simulator to analyze the performance of the GGF technique in comparison to an open-loop control scheme. The simulator mimicked the drop-by-drop deposition of build material, similar to that of a drop-on-demand RP system.

5.2 Computational representation of physical spaces

In the physical world, the target object, the droplets and the deposition field all are continuous spaces. However, for the purposes of simulation, $T(x,y)$, $D(x,y)$ and $A(x,y,t)$ were all represented as discrete spaces by matrices **T**, **D**, and $\mathbf{A}_n$, respectively. These matrices, or heightmaps, were essentially spatial sub-samples of their corresponding physical spaces, where **T**, **D** and $\mathbf{A}_n$ represent the target geometry, droplet geometry and actual geometry at the nth iteration of the algorithm, respectively. The "physical resolution," e, is the distance in the physical world that each of the matrixes' discrete element-to-element intervals represent. We simulate the physical printing procedure by tracking printed matter at the resolution, e, which is finer than the resolutions of Q and q.

While physical spaces are represented as heightmaps in these simulations, it should be noted that not all 3D objects can be represented as such, due to features like overhangs or internal cavities. The heightmap representation was used for computational simplicity, but the representation could be generalized by using voxel or parametric representations. That is, a top-down 2.5D geometric representation was used for these simulations; however, this same algorithmic principle could be represented in a fully 3D geometric model such as a voxel representation, or a parametric representation in which the geometry is explicitly modeled with equations.

5.2.1 Intended target object heightmap

The matrix **T** was created by sub-sampling $T(x,y)$ at the simulation resolution, e (Figure 3). Each sample point is e units in physical space away from one another.

5.2.2 Single droplet heightmap

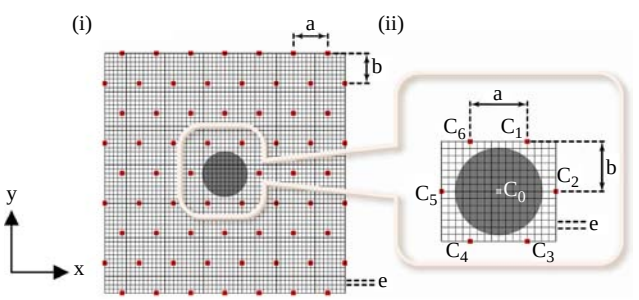
The liquid droplet shape associated with RP techniques can be mathematically approximated using a lens model, as explained in prior literature (Doumanidis and Skordeli, 2000). Therefore, an approximation for the surface of a single droplet is:

$$\hat{D}(x,y) = \sqrt{r^2 - (x-(X-u)) - (y-(Y-v))} + w \qquad (4)$$

where r is the radius of curvature; X and Y are the lens' center coordinates; u and v are the deviations of the actual droplet center from the intended center due to process error; w is the lens' center-to-substrate offset (Figure 4). Note that u and v represent the translation of the droplet relative to the deposition tip's location, i.e. natural deviation from the intended droplet center due to physical process errors.

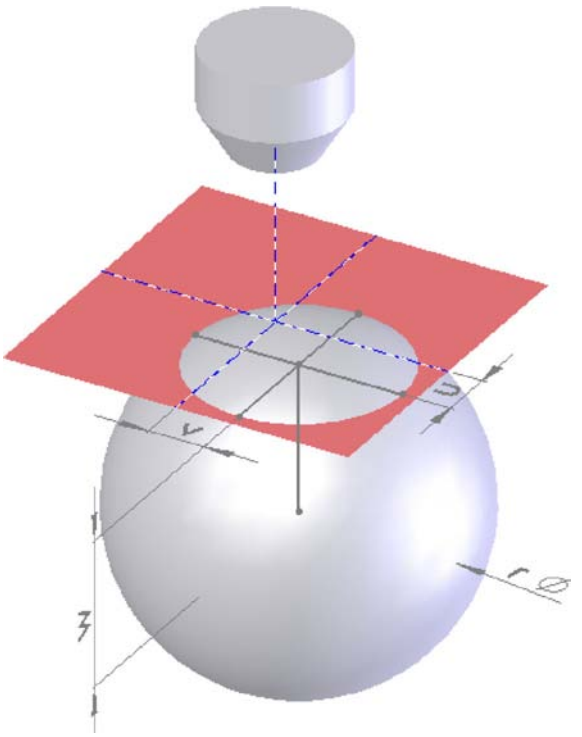
Given the lens parameters, equation (4) can be used to generate a matrix that approximates the surface of the droplet.

Figure 3 Physical resolution



Notes: Overlay of physical resolution matrices on the global selection space (i); the local selection space (ii)

Figure 4 Diagram of droplet parameters



Notes: The deposition tool nozzle above the substrate and the underlying droplet modeled as a lens; also shown: the corresponding truncated sphere and associated parameters u, v, w, and r

This surface can be sub-sampled at the resolution, e, to create the heightmap of the nth droplet, $\mathbf{D}_n$:

$$[\boldsymbol{D}]_n = \begin{bmatrix} \hat{D}(0,0) & \hat{D}(e,0) & \hat{D}(2e,0) & \cdots & \hat{D}(C\cdot e,0) \\ \hat{D}(0,e) & \hat{D}(e,e) & \hat{D}(2e,e) & & \\ \hat{D}(0,2e) & \hat{D}(e,2e) & \hat{D}(2e,2e) & & \\ \vdots & & & \ddots & \\ \hat{D}(0,R\cdot e) & & & & \hat{D}(C\cdot e,R\cdot e) \end{bmatrix} \qquad (5)$$

where $\hat{D}$ is a function of the lens parameters: r_n, X_n, u_n, Y_n, v_n and w_n. R and C represent the number of rows and columns of the matrix (i.e. size) required to describe the simulated X-Y plane.

5.2.3 Deposition field heightmap

The deposition field immediately after the nth droplet has been deposited can be represented with the heightmap, $\mathbf{A}_n$:

$$[\boldsymbol{A}]_n = \begin{bmatrix} A(0,0,t_n) & A(e,0,t_n) & A(2e,0,t_n) & \cdots & A(C\cdot e,0,t_n) \\ A(0,e,t_n) & A(e,e,t_n) & A(2e,e,t_n) & & \\ A(0,2e,t_n) & A(e,2e,t_n) & A(2e,2e,t_n) & & \\ \vdots & & & \ddots & \\ A(0,R\cdot e,t_n) & & & & A(C\cdot e,R\cdot e,t_n) \end{bmatrix} \qquad (6)$$

where t_n is the time just after the nth droplet has been deposited.

5.3 Simulation flow

The core of the simulation is the iterative update of the deposition field heightmap, $\mathbf{A}_n$. Since $\mathbf{A}_n$ represents the physical space in which the print is occurring, the $\mathbf{A}_n$ heightmap reflects the results of all algorithmic decisions as well as the effects of process uncertainties. The simulation begins with $\mathbf{A}_n$ as a matrix of zeros.

Then a seed droplet, D_1, is generated by using the lens parameters: r_1, u_1, v_1 and w_1. The seed droplet's center coordinates (X_1,Y_1) are randomly selected from points in the global selection space. The first droplet is deposited in simulation by superimposing the droplet matrix, $\mathbf{D_1}$, over the deposition field matrix, $\mathbf{A}_0$:

$$[\mathbf{A}]_1 = [\mathbf{A}]_0 + [\mathbf{D}]_1 \tag{7}$$

Once the seed droplet has been deposited into the deposition field, the main iterative portion of Local-GGF commences. In order to choose the location of the second droplet, (X_2,Y_2), the local selection space is constructed. The set, q_n, represents the local selection space just before the nth droplet is deposited:

$$q_2 = \left\{ C_0 \quad C_1 \quad C_2 \quad C_3 \quad C_4 \quad C_5 \quad C_6 \right\}_2 \tag{8}$$

The scores of the candidates in the local selection space are generated:

$$\begin{aligned} S(q_2) &= \left\{ S(C_0)\ S(C_1)\ S(C_2)\ S(C_3)\ S(C_4)\ S(C_5)\ S(C_6) \right\}_2 \cdots \\ &= \left\{ T\left[\frac{C_i}{e}\right] - A\left[\frac{C_i}{e}\right]_1 | i \in Z,\ 0 \le i \le 6 \right\} \end{aligned} \tag{9}$$

where C_i represents the $(x,y)_i$ coordinates (i.e. location of the ith candidate location in physical space), and $C_i/e = (x/e,\ y/e)_i$ (i.e. location of the ith candidate location represented in terms of $A[\ ]$'s matrix indexes).

The location of the next droplet is selected by choosing the candidate with the highest score, and the droplet is deposited in simulation by superimposing the matrixes:

$$[\mathbf{A}]_2 = [\mathbf{A}]_1 + [\mathbf{D}]_2 \tag{10}$$

These steps are repeated, whereby:

$$\begin{aligned} q_n &= \left\{ C_0 \quad C_1 \quad C_2 \quad C_3 \quad C_4 \quad C_5 \quad C_6 \right\}_n \\ &= \left\{ (X_{n-1}, Y_{n-1}) \left(X_{n-1} + \frac{a}{2}, Y_{n-1} + b \right) (X_{n-1} + a, Y_{n-1}) \right. \\ &\quad \times \left(X_{n-1} + \frac{a}{2}, Y_{n-1} - b \right) \left(X_{n-1} - \frac{a}{2}, Y_{n-1} - b \right) \\ &\quad \left. \times (X_{n-1} - a, Y_{n-1}) \left(X_{n-1} - \frac{a}{2}, Y_{n-1} + b \right) \right\}_n \end{aligned} \tag{11}$$

$$S(q_n) = \left\{ T\left[\frac{C_i}{e}\right] - A\left[\frac{C_i}{e}\right]_{n-1} | i \in Z, 0 \le i \le 6 \right\} \tag{12}$$

$$[\mathbf{A}]_n = [\mathbf{A}]_{n-1} + [\mathbf{D}]_n = [\mathbf{A}]_0 + \sum_{k=1}^{n} [\mathbf{D}]_k \tag{13}$$

For each set of simulation parameters, a range of heuristic score thresholds, L, were tested to find near-optimal performance of the Local-GGF process. The threshold that yielded the lowest root mean square (RMS) surface height error was selected. The optimal heuristic score thresholds varied from case-to-case and are listed in Section 8 where appropriate.

The simulation ends when end condition equation (3) has been satisfied:

$$\begin{aligned} &(T[r,c] - A[r,c]) \le L, \quad \text{where } r \in Z, 0 \le r \le R \\ &\quad \text{and} \quad c \in Z, 0 \le c \le C \end{aligned} \tag{14}$$

where r and c are the matrix indexes, and $T[\ ]$ and $A[\ ]$ are of size R by C.

The same simulation engine was used for Global-GGF, except that the top 50 percent of the candidates in the global selection space were selected for subsequent deposition during each iteration.

5.4 Modeling of process uncertainty

Process uncertainties that occur at the droplet-shape level, were incorporated into the simulations by randomly drawing the r, u, v and w parameters from normal distributions; $r \sim N(r_{\text{nom}},\sigma_r)$, $u \sim N(u_{\text{nom}},\sigma_u)$, $v \sim N(v_{\text{nom}},\sigma_v)$ and $w \sim N(w_{\text{nom}},\sigma_w)$, where σ_r, σ_u, σ_v, σ_w, r_{nom}, u_{nom}, v_{nom} and w_{nom} are user-defined parameters of the r, u, v and w distributions. Variation in the r parameter represents uncertainty in the radius of curvature of the droplets. Uncertainty in the x-y positioning of droplets is represented by variation in u and v. The variation in w represents uncertainty in the maximum droplet thickness.

Process uncertainties that occur on the overall part-shape level (e.g. during-print part deformation due to melting), can be incorporated by applying a morphological filter to $\mathbf{A}_n$ during each iteration after the $\mathbf{D}_n$ matrix is superimposed. The morphological filter used in this paper is a 2D linear filter that uniformly averages over a specified radius of pixels.

While these simulated process uncertainties do not capture all existing physical possibilities, they do serve as a representative set.

5.5 Simulation parameter selection

The droplet parameters r_{nom}, u_{nom}, v_{nom} and w_{nom} were selected based upon suggested values in prior literature (Doumanidis and Skordeli, 2000) (Table I).

These parameter values result in a droplet radius of 4 mm and a droplet maximum height of 2 mm. The values of σ_r, σ_u, σ_v, σ_w and the score threshold, L, were experimentally varied throughout the following simulation experiments.

Next, an optimal value for the droplet center-to-center spacing had to be determined, which yielded minimal surface height variations when droplets were hexagonally packed. The spacing necessary for the midpoint between droplet centers to have a height equal to the height of the droplet centers was:

$$\sqrt{3r^2 + 2rw - w^2} = \sqrt{3 \cdot 5^2 - 2 \cdot 5 \cdot 3 - (-3)^2}[\text{mm}] = 6\,\text{mm} \tag{15}$$

The a, b and e parameters were coupled and had to be chosen carefully. In order for the droplets to hexagonally pack, the

Table I Droplet parameter values

r_{nom}	u_{nom}	v_{nom}	w_{nom}
5 mm	0 mm	0 mm	−3 mm

a and b values had to be in a $2/\sqrt{3}:1$ ratio. However, in order to have the hexagonally packed droplets' centers perfectly align with the square-packed matrix, $\mathbf{A}_n$, the a and b intervals had to be multiples of e. One set of a and b values that were multiples of e and yet still closely approximated a $2/\sqrt{3}:1$ ratio, was $a = 8e$, $b = 7e$. Given that the center-to-center spacing, a, had to be 6 mm [as shown above in equation (15)], e and b were then fixed to 0.75 and 5.25 mm, respectively.

5.6 Simulation of open-loop control

The simulator for the open-loop SFF technique was very similar to that for the GGF case. However, the iterative decision making was replaced by a list of points that corresponded to the locations for droplet centers, i.e. a tool path plan. This list was generated by filling the intended target geometry with the nominal droplet-shaped structuring element, until all points on the surface had heights greater than or equal to $T(x,y)$. Droplets, $\mathbf{D}_n$, were then placed in $\mathbf{A}_n$ for each point in the list.

6. Physical test platform for GGF (proof-of-concept implementation)

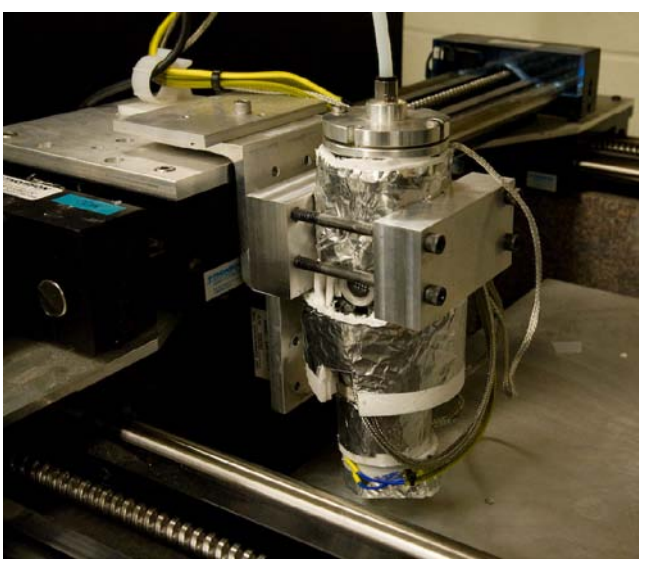
6.1 Overview

In order to validate the concepts proposed above, and also to address the feasibility of physically implementing the control scheme, a physical test platform was developed to demonstrate the GGF control technique (Figure 5).

6.2 System design

A custom SFF test platform was developed to implement and test the GGF technique; in addition to performing GGF prints, the system was also capable of performing open-loop prints under similar test conditions. By controlling the print conditions and inducing specific forms of process uncertainty, the performance of different control schemes could be studied.

Figure 5 Physical experimentation platform



Note: Custom wax deposition tool mounted on *X-Y-Z* gantry robot

6.2.1 Positioning system

We designed and built a custom gantry positioning system comprising two coupled linear actuators along the *X*-axis, one along the *Y*-axis and one along the *Z*-axis (Aerotech, Inc.). The positioning system was capable of moving at accelerations up to 20 m/s^2. The system has a positioning accuracy and repeatability of 25 μm. The custom-fabricated granite base reduced structural vibration and ensured accurate tool positioning.

6.2.2 Deposition tool

The custom-designed and fabricated deposition tool was a paraffin drop-on-demand tool. A 0.007-inch diameter VHS-M jet valve (INKX05153350AA; Lee Company) was attached to a custom-fabricated aluminum liquid reservoir through a Minstac male-to-male connector (INZX0530650AA; Lee Company) and an in-line 12 μm filter (INMX0350000AA; Lee Company). The aluminum reservoir heated with a 200 W band heater and monitored with a band-mounted J-type thermocouple. The reservoir was also pressurized in an air-over-liquid fashion at 12 psi.

A 5 V control signal was output from the controlling PC through a digital I/O board and fed into a spike-and-hold valve controller (IECX0501350A; Lee Company) which provided the proper electrical control signal to the valve.

6.2.3 Metrology

Measurements of the printed part height were used during closed-loop prints as part of the GGF algorithm, as well as for quantifying part height error after the completion of both closed- and open-loop prints.

While future implementations would ideally monitor the heights of neighboring candidates simultaneously in real-time, in this proof-of-concept implementation, the neighboring candidate heights were measured serially by a single-point height sensor. The sensor used in this system was a CMOS laser triangulation range sensor (Microtrak II, MTI Instruments, Inc.).

The sensor had a range of 10 mm, a spot size of 30 μm, and a resolution of 1.25 μm. The sensor output an analog signal, which was read-in by the controlling PC through an analog-to-digital converter.

6.2.4 Control software

A custom-written control program was developed in C++ to execute the GGF and open-loop control sequences. Aerotech C++ libraries were integrated to handle low-level motion control operations and sensor I/O.

6.3 Implementation considerations

Several practical issues had to be addressed during the implementation of the feedback control scheme. First, due to the parallax between the laser beam and laser sensor, tall vertical parts sometimes were difficult to measure; the vertical edges of the parts occasionally hid the laser beam from its own laser sensor. This problem is not a fundamental limitation of the GGF control scheme, rather, it was a practical concern of this particular proof-of-concept implementation. However, by printing parts with smoother surfaces, adverse effects caused by this issue were avoided.

Another practical issue encountered was the size of the droplets produced by the deposition tool. The lower limit of the control system's valve signal was 1 ms. Given the particular valve used, and the minimum reservoir pressure (dictated by a threshold below which the fluid pooled instead of jetted), the droplet was

restricted to diameters on the order of approximately 1 mm. Again, this is not by any means a fundamental limitation of the control algorithm itself. Furthermore, the conceptual validity and feasibility of implementation can be demonstrated with this platform regardless of the particular droplet size. On a side note, the size of the droplets resulted in a thermal mass which yielded droplets that took about one second to set, and about three seconds to freeze. The larger the droplets the more they retained heat due to their increased mass, and thus, the longer they took to freeze. Consequently, the time between droplets had to be selected accordingly to ensure subsequently droplets were not deposited on top of molten droplets.

It is important to note that this experimental SFF platform was intended to demonstrate the physical implementation of the control algorithm and is a proof-of-concept. No claims are being made about the optimality of the platform as a high-throughput SFF system, rather, we are only making claims about the algorithm itself.

6.4 Induced process uncertainties

We induced process uncertainties in several ways. In order to induce uncertainty in the droplet size, which represents uncertainty in the material properties of the build-material, we varied the hold time of the valve by adding a Gaussian random term to the nominal hold time of 4 ms.

In order to represent uncertainty of the substrate geometry, we printed samples on top of acrylonitrile-butadiene-styrene (ABS) plastic constructs to create non-flat print substrates.

6.5 Print parameter selection

We determined the nominal valve hold time based upon the desired droplet size. The drop-to-drop distance was empirically determined based upon which spacing yielded a line of droplets of constant height. If the spacing was too small, the line of droplets would be discontinuous. If the spacing was too great, the droplets would overlap and the height of the printed line would continue to increase resulting in a line with a non-flat surface.

The time between droplets was empirically determined to be four seconds to ensure that droplets were not being deposited on top of a molten surface. While this is not optimized for efficiency and speed, we needed to ensure solidification of the substrate since we were primarily concerned with measuring the resultant geometric fidelity.

7. Performance evaluation methodology

We used an open-loop SFF process (no feedback control) as a baseline for comparison in both the simulation and physical experiments.

The quantitative metric used for comparison was the RMS surface error between the actual printed surface and the theoretically intended surface. This was calculated via a simple point-by-point comparison of the actual and intended surfaces:

$$\text{RMS error} = \sqrt{\frac{1}{R \cdot C}\sum_{j=1}^{R}\sum_{i=1}^{C}(T[i,j] - A[i,j])^2} \qquad (16)$$

7.1 Methodology for simulation experiments

In simulation, the GGF technique's performance was compared to that of the open-loop baseline by simulating the print of three different target shapes with both GGF and open-loop control schemes. The three target shapes chosen were:

1 a rectangular prism;
2 a dome; and
3 an ovine meniscus cartilage.

For each control scheme and each target shape, the RMS surface error was measured under four types of process uncertainty (as discussed in Section 5.4). These four types of process uncertainty were:

1 droplet radius of curvature;
2 droplet thickness;
3 droplet placement; and
4 during-print part deformation of the part.

To test the control scheme under uncertainty in droplet radius, the droplet radius was varied during simulation by adding a random radius offset to the nominal radius dimension, r. The distribution of this random offset was characterized by the standard deviation (SD) of this random variable (i.e. the radius offset). To test under varying levels of uncertainty in radius, this random variable's SD was varied from root mean square (no uncertainty in the radius) to 1.5 mm.

Similarly, to test the control scheme under uncertainty in droplet thickness, a random offset was added to the parameter, w. To test under varying levels of uncertainty in droplet thickness, the SD of the random offset was varied from root mean square (no uncertainty in droplet thickness) to 1.5 mm.

To test under varying levels of uncertainty in droplet placement, a random offset was added to the u and v parameters; the SD of this offset was varied from 0 to 6 mm.

To simulate the fourth type of uncertainty, during-print part deformation, the linear morphological filter was applied to the geometric model after each iteration of the simulation. To simulate varying levels of during-print part deformation, the radius of the filtering element was varied from 0 to 3 mm.

Each simulation was conducted three times under identical conditions, and then the results were averaged by taking the arithmetic mean.

7.2 Methodology for physical experiments

In the physical experimentation, the target shape was a 5 mm tall dome with a radius of curvature of 12 mm. Both GGF and open-loop were tested on the dome target shape, and the RMS surface error was measured under:

- no induced error;
- a variation in valve time with a SD of 20 ms; and
- a non-flat substrate representing situation/environmental uncertainty (the print was conducted on top of an ABS plastic dome of radius 12 mm and height 3 mm).

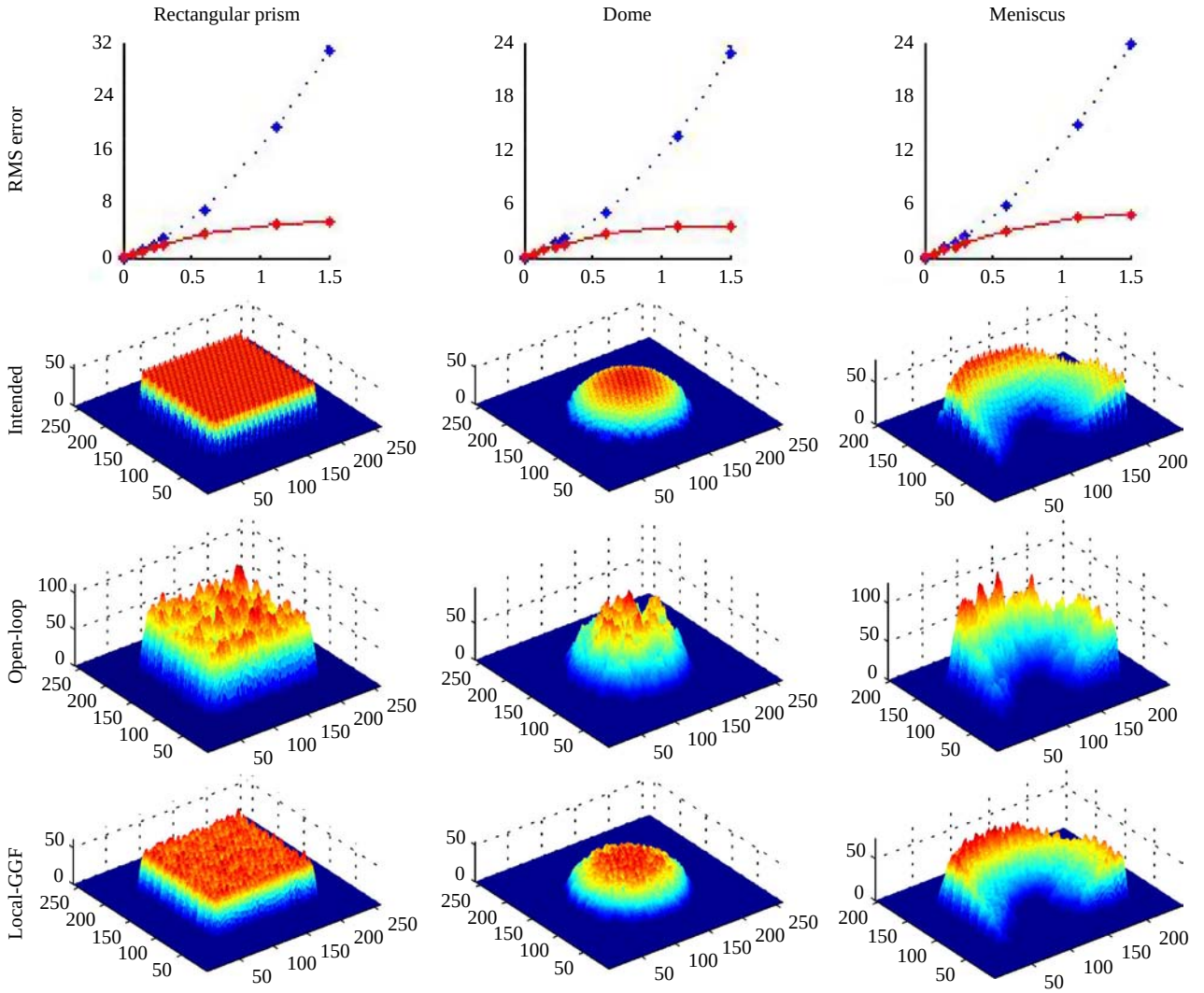
The RMS surface error calculation was made based upon a 0.2 mm resolution laser scan of the complete printed object, which was conducted at the conclusion of each scan. Point-to-point comparison between the scan of the printed component and the intended geometry was conducted to perform the calculation.

8. Simulation results and discussion

8.1 Case 1 – varying uncertainty in droplet radius of curvature

The RMS errors were smaller for Local-GGF than for open-loop control for all shapes and all degrees of uncertainty in the radius of curvature (Figure 6). Local-GGF's RMS error appeared to asymptotically level-off whereas the open-loop

Figure 6 Performance comparison with uncertainty in droplet radius of curvature



Notes: Row 1, RMS error of printed surface (mm) vs SD of droplet radius of curvature distribution (mm) (dotted line, open loop; solid line, Local-GGF); rows 2-4, surface plots of intended and printed geometries (mm) with SD of radius of curvature uncertainty equal to 1.125 mm

error appeared to grow exponentially. With a 1.125 mm SD in the radius of curvature distribution (28 percent of the nominal radius of curvature), the Local-GGF RMS error was 74, 74 and 70 percent less than the open-loop error for the rectangular prism, dome and meniscus, respectively. This disparity in performance grew as the uncertainty in radius increased.

The error growth of the open-loop case seems to grow exponentially as the radius of curvature, and hence the droplet volume, become less certain. As the uncertainty increases, so does the mean droplet volume, which contributes to fast growth of the RMS error in open loop. The error growth for GGF appears to slow as uncertainty increases, due to the error fighting behavior of the algorithm.

8.2 Case 2 – varying uncertainty in droplet thickness

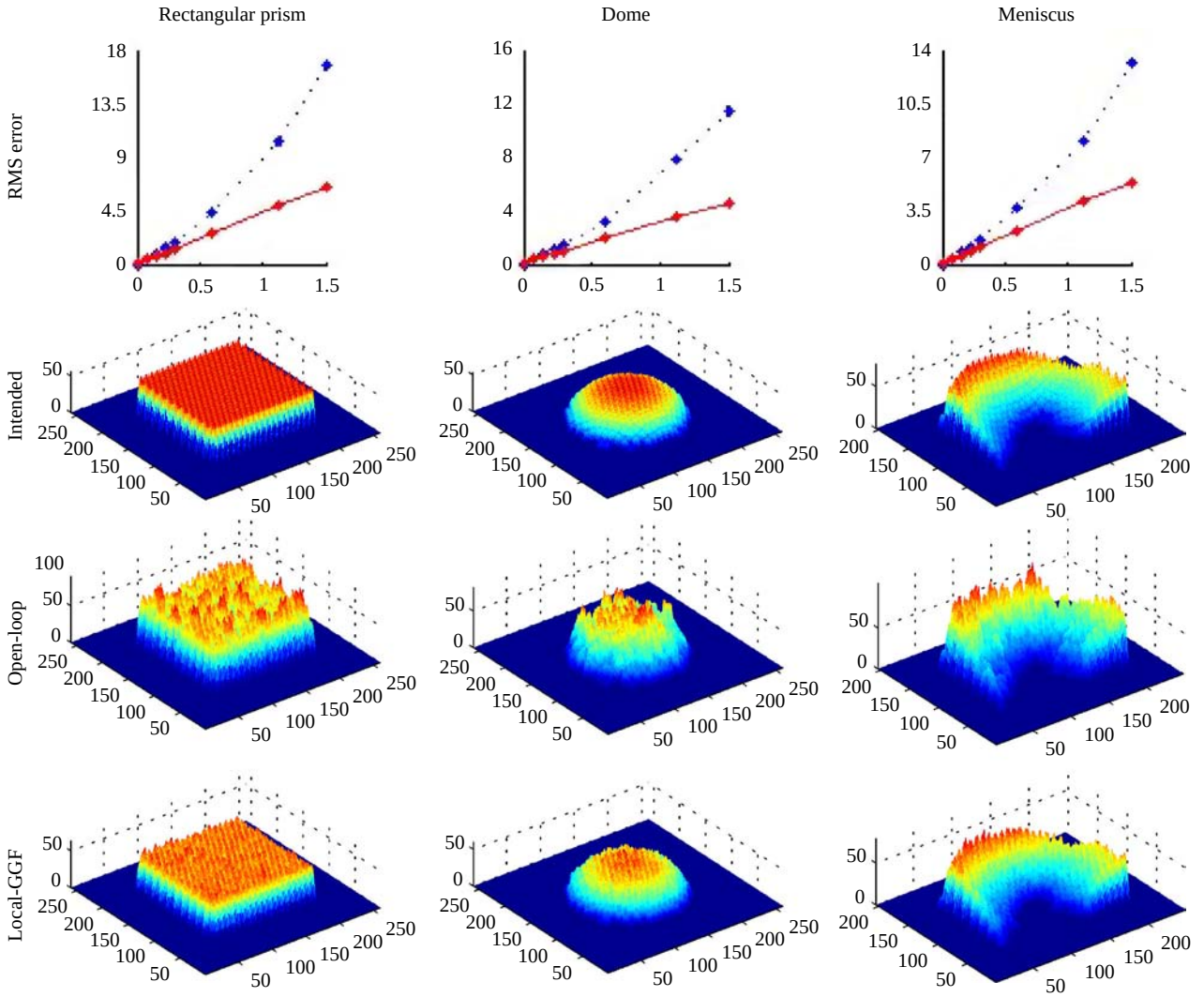
The RMS errors were smaller for Local-GGF than for open-loop control for all shapes and all degrees of uncertainty in the droplet thickness (Figure 7). GGF's RMS error appeared to grow linearly, whereas the open-loop error seemed to grow exponentially. With a 1.125 mm SD in the droplet thickness distribution (56 percent of the nominal droplet thickness), the Local-GGF RMS error was 51, 55 and 49 percent less than the open-loop error for the rectangular prism, dome and meniscus, respectively. This disparity in performance grew as the uncertainty in droplet thickness increased.

As in the previous case, as uncertainty in the droplet thickness increases, so does uncertainty in the droplet volume. As this uncertainty increases, the mean droplet volume grows, which leads to rapidly increasing RMS error for open-loop. Again, GGF error grows less quickly and the error growth slows (although this slowing is much less pronounced than in the prior case).

8.3 Case 3 – varying uncertainty in droplet placement

The RMS errors were smaller for Local-GGF than for open-loop control for all shapes and all degrees of uncertainty in X-Y droplet placement (Figure 8). Both GGF and

Figure 7 Performance comparison with uncertainty in droplet thickness.



Notes: Row 1, RMS error of printed surface (mm) vs SD of droplet thickness distribution (mm) (dotted line, open loop; solid line, Local-GGF); rows 2-4, surface plots of intended and printed geometries (mm) with SD of droplet thickness uncertainty equal to 1.125 mm

open-loop RMS error grew with asymptotic behavior; however, the GGF error was less than that of the open-loop control. With a 2 mm SD in the droplet translation distribution (25 percent of the nominal droplet diameter), the Local-GGF RMS error was 14, 20, and 11 percent less than the open-loop error for the rectangular prism, dome and meniscus, respectively.

The less-pronounced disparity between open-loop and GGF is likely due to the noise averaging characteristics of a positional error centered about the intended droplet location. This disparity would be more pronounced in unidirectionally biased circumstances.

8.4 Case 4 – time-varying deformation of printed objects

The RMS errors were smaller for Local-GGF than for open-loop control for all shapes and all degrees of during-print part deformation (Figure 9). With a 3 mm radius filter acting over the first one-eighth of the nominal open-loop print duration, the Local-GGF RMS error was 48, 50 and 52 percent less than the open-loop error for the rectangular prism, dome and meniscus, respectively.

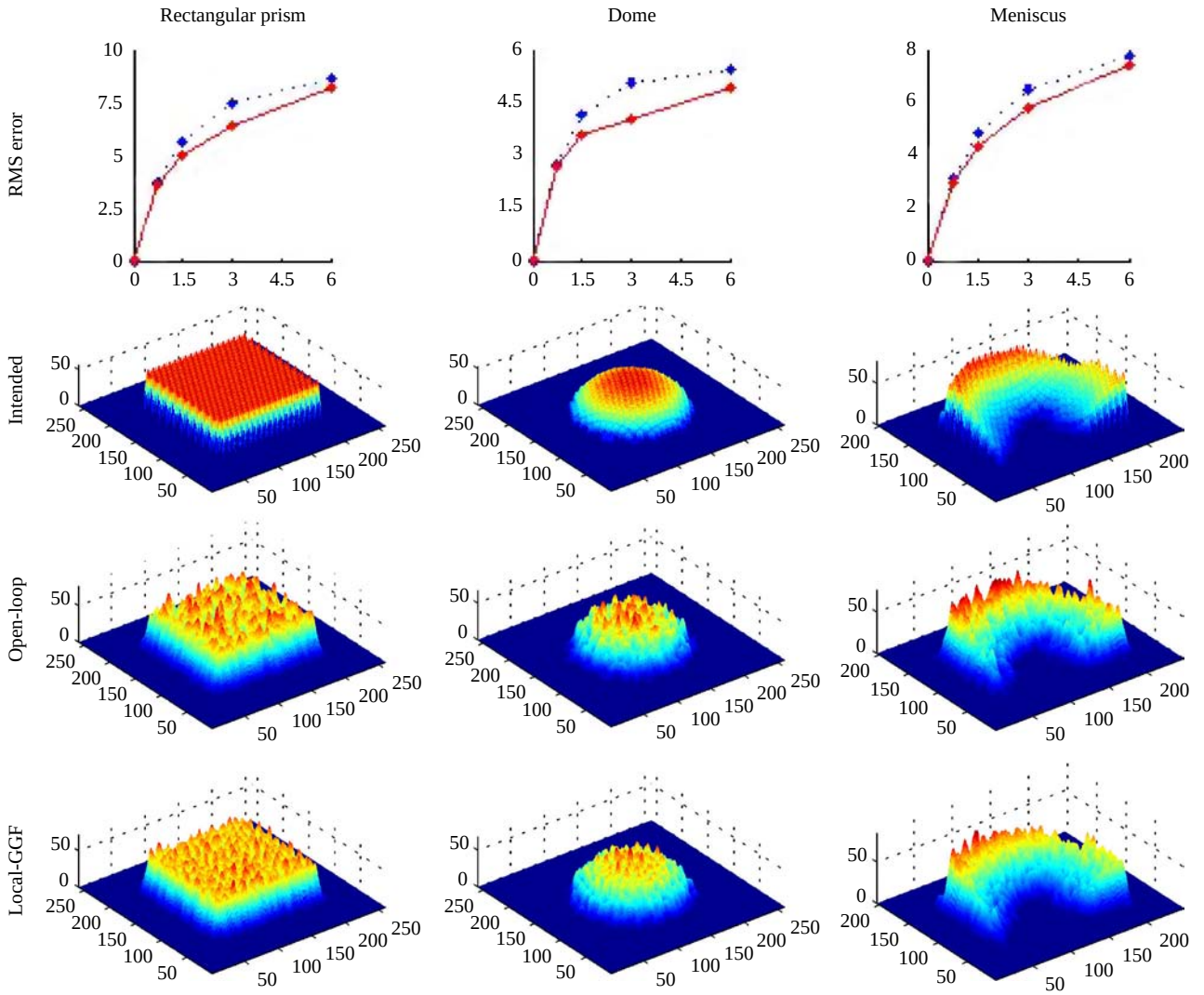
The disparity between open-loop and GGF grew rapidly, and conceivable could grow to infinity; in an extreme case, a temporary melting effect could nearly annihilate the open-loop part, but be nearly fully restored by GGF.

The nature of this growth, and the specific shape of the error growth, is entirely dependent on the specific details of the type of time-varying deformation imposed. For example, melt would have an entirely different behavior from evaporation.

8.5 Case 5 – investigation of Global-GGF, 4/6/8 connectivity (simulation of droplet misfiring)

A simulation experiment was conducted to gain basic insight into the performance of alternative implementations of GGF:

Figure 8 Performance comparison with uncertainty in droplet placement.



Notes: Row 1, RMS error of printed surface (mm) vs SD of placement distribution (mm) (dotted line, open loop; solid line, Local-GGF]; rows 2-4, surface plots of intended and printed geometries (mm) with SD of placement uncertainty equal to 3 mm

Global-GGF versus Local-GGF, and 4/8-connectivity instead of six-connectivity.

In this experiment, a 10 mm (H) X 30 mm (W) X 30 mm (L) rectangular prism was printed with 1 mm diameter, 0.1 mm thick droplets. The droplet would fail to fire a certain percentage of instances in which it was commanded to fire.

As Figure 10 shows, in terms of RMS error, Global-GGF appears to behave in a very similar nature to Local-GGF. In fact, in simulation, they were indistinguishable. Furthermore, in terms of RMS error, four-connectivity vs eight-connectivity has no effect. The square lattice packings (four- and eight-connectivity) present slightly different results from hexagonal packing (six-connectivity), but this difference is more a property of packing behavior of droplets than it is a reflection of the GGF algorithm.

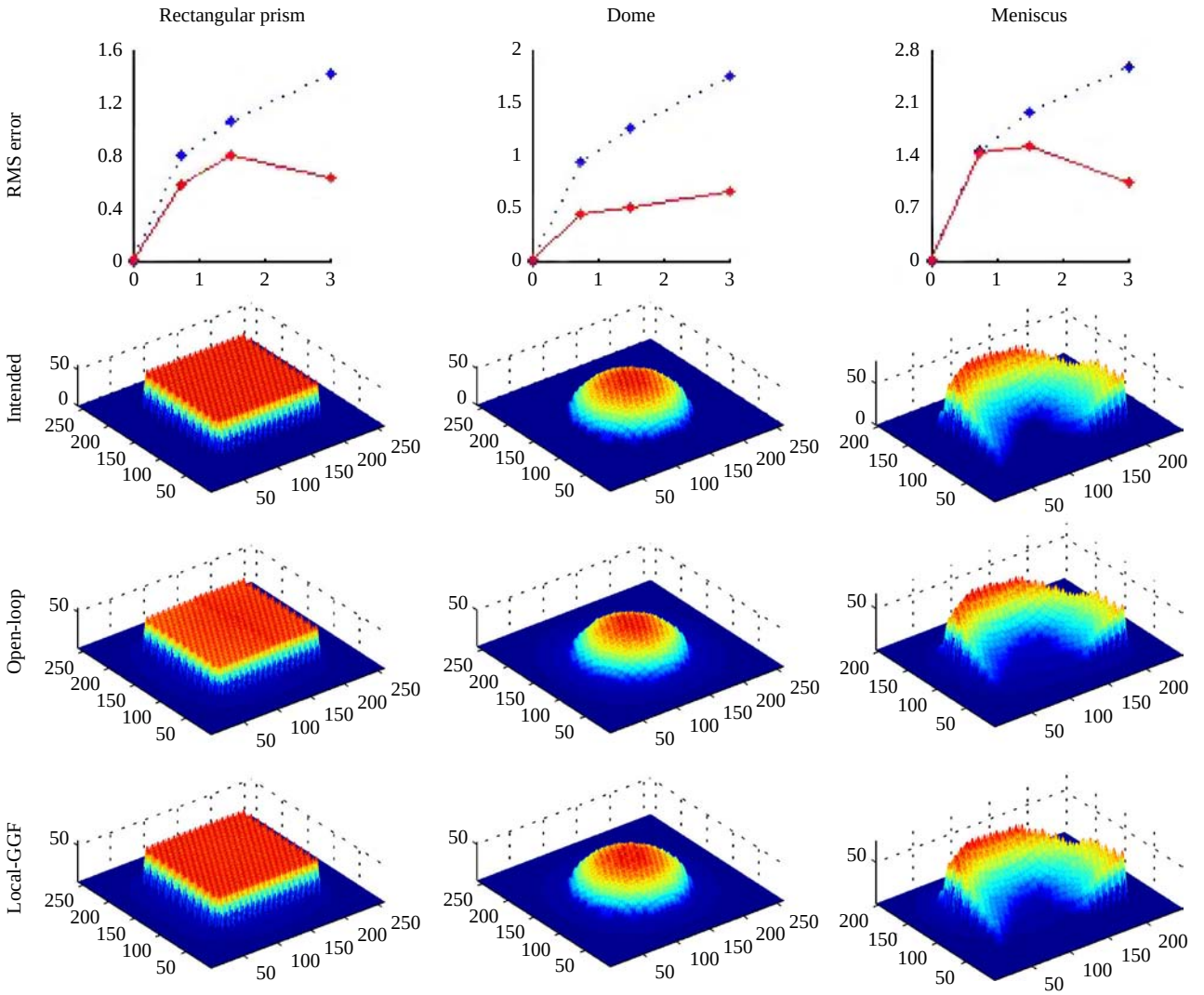
It is not surprising that there is not distinguishable difference in terms of geometric fidelity between Local-GGF and Global-GGF, as the latter is merely a parallelized version of the former.

8.6 Cost of geometric feedback scanning

In simulation, we tracked the number of times a droplet was deposited (and hence the number of times the local selection space was scanned in Local-GGF), as well as the number of times a global selection space scan was conducted (during Global-GGF or for the re-insertion point searches of Local-GGF) (Figures 11 and 12). Some types of uncertainty create more of a scanning expense than others.

For example, in Case 5, when droplets fail to fire a certain percentages of the time, the GGF algorithm keeps working in an attempt to fight the error. Even in the extreme circumstance when droplets fail to fire with a 95 percent probability, GGF will not cease until it successfully combats the error. On the other hand, as a result of its incessant error fighting, the print continues much longer than in the

Figure 9 Performance comparison with during-print part deformation



Notes: Row 1, RMS error of printed surface (mm) vs radius of morphological filtering element (mm) (dotted line, open loop; solid line, Local-GGF); rows 2-4, surface plots of intended and printed geometries (mm) with filtering radius set at 3 mm

open-loop case and the overall scanning cost and print duration rises accordingly. Of course, however, along with open-loop's shorter and less expensive run (since it ends as scheduled without ever detecting an error) comes the lowered geometric fidelity. To a certain extent, the increased duration of print and cost of scanning is the unavoidable price to pay for increased geometric fidelity.

At a certain point (above 60 percent or so) it becomes a question of how important geometric fidelity is to the user. The duration of Local-GGF scales with the number of droplets and the duration of Global-GGF scales with the number of global selection space scans: both grow exponentially and become substantially large above the 60 percent point.

However, contrary to the rising cost of scanning seen in Case 5, in Case 2 with a positive-biased uncertainty in droplet thickness, the cost of scanning reduces with increased uncertainty. Since the uncertainty adds more material than anticipated, the uncertainty only brings the part closer to its intended geometry faster (Figures 13 and 14). Again, open-loop is not aware of the additional build-material and continues its print longer than it should; as scheduled a priori.

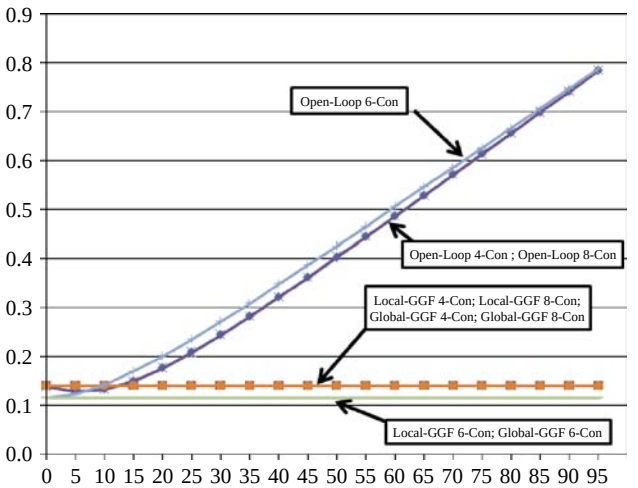
9. Physical experimentation results and discussion

9.1 Case 1 – no induced process uncertainty

The baseline case was one in which both open- and closed-loop prints of a dome were performed. The GGF algorithm did not require the tuning of any control parameters (beyond droplet-to-droplet spacing which was identical to that used for the open-loop control). However, the open-loop algorithm required the determination of nominal layer thickness.

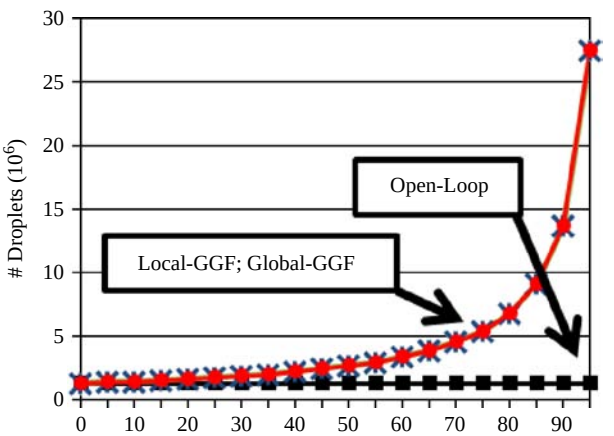
A 10 × 10 mm, 11-layer cube was printed to estimate the nominal layer thickness. By dividing the actual cube height by the number of layers, the resulting estimated layer thickness was

Figure 10 RMS error normalized to maximum part height vs percentage of attempted droplet firings with no droplet fired



Note: Error growth shown for all implementations of GGF and open-loop control schemes

Figure 11 Number of droplets fired during "no-fire" experiment



Note: Number of droplets vs probability of attempted droplet firing resulting in no droplet fired

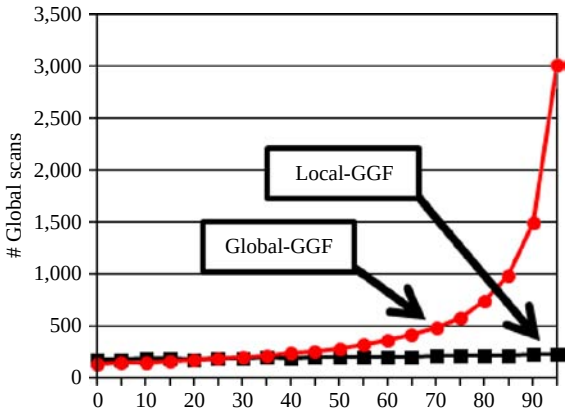
0.60 mm. However, the resulting printed dome was too tall; the surface exhibited an RMS error of 1.98 mm. Therefore, another round of layer thickness estimation was conducted on a printed dome (as opposed to the cubic test piece). Now, with complete a priori knowledge, the estimate of layer thickness obtained was more accurate (1.04 mm) and resulted in a printed dome that more closely resembled the target geometry. The open-loop print conducted with a priori knowledge exhibited an RMS surface error of 0.58 mm (Figure 15).

The Local-GGF print, without a priori knowledge of the layer thickness printed the dome with the same geometric fidelity (as determined by RMS surface error), 0.59 mm.

9.2 Case 2 – variation in valve hold time

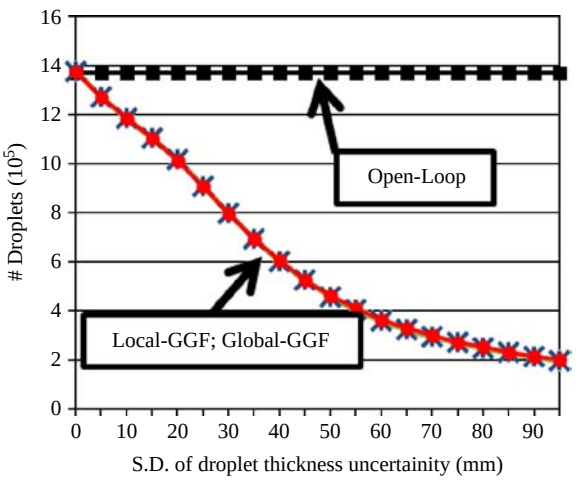
When a positive random variable was added to the nominal hold time (SD of 0.020 ms), this mimicked a native process uncertainty in the droplet volume. The open-loop printed dome exhibited an RMS surface error of 1.33 mm; the

Figure 12 Number of global scans during "no-fire" experiment



Note: Number of global scans conducted vs probability of attempted droplet firing resulting in no droplet fired

Figure 13 Number of droplets fired during "positive-biased uncertainty in droplet thickness" experiment



Note: Number of droplets vs probability of attempted droplet firing resulting in no droplet fired

Local-GGF printed dome exhibited an RMS surface error of 0.69 mm (Figure 16).

9.3 Case 3 – non-flat substrate

When the dome was printed on top of an ABS spherical-lens substrate (1 mm H × 6 mm D), the open-loop print exhibited an RMS surface error of 1.16 mm; the Local-GGF dome had an error of 0.36 mm (Figure 17).

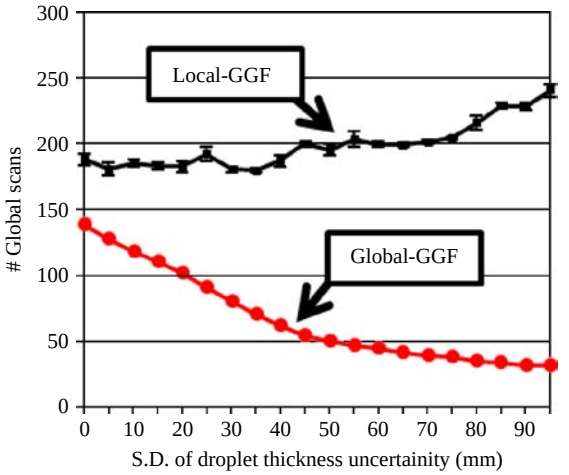
9.4 Case 4 – reduced deposition tool pressure

When the pressure of the deposition tool's reservoir was reduced to 8 psi while holding the droplet-to-droplet spacing constant (mimicking a natural variation in system conditions), the resultant droplets were smaller. The open-loop printed dome had an RMS surface error of 2.57 mm; the Local-GGF maintained an error of only 0.34 mm (Figure 18).

10. Conclusions

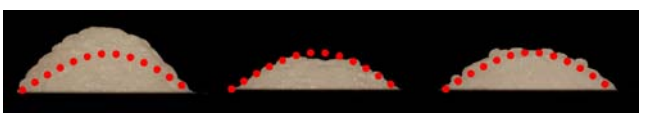
The results presented in this paper demonstrate that GGF consistently performs more effectively than open-loop control.

Figure 14 Number of global scans during "positive-biased uncertainty in droplet thickness" experiment



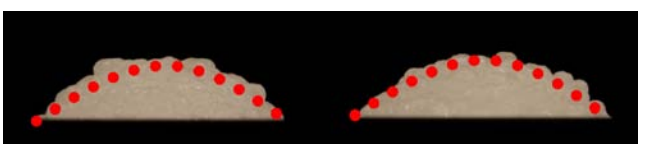
Note: Number of global scans conducted vs probability of attempted droplet firing resulting in no droplet fired

Figure 15 Photographs of printed dome constructs



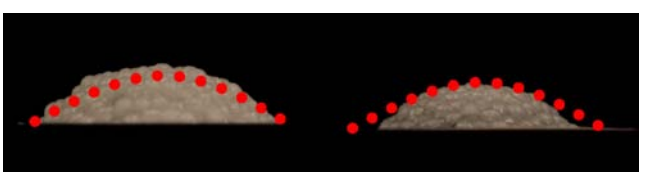
Notes: Left, openloop with partial a priori knowledge; center, open-loop with complete a priori knowledge; right, Local-GGF

Figure 16 Photographs of printed dome constructs



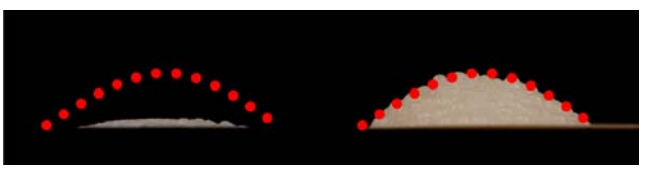
Notes: Left, openloop; right, Local-GGF

Figure 17 Photographs of printed dome constructs



Notes: Left, openloop; right, Local-GGF

Figure 18 Photographs of printed dome constructs



Notes: Left, openloop; right, Local-GGF

The degree to which it improves performance depends on the type and the extent of process uncertainty.

In simulation, several conclusions can be reached about the nature of the proposed control scheme. While the disparity between GGF and open-loop control keeps increasing as the uncertainties in radius of curvature and droplet thickness increase, the disparity is less pronounced with respect to uncertainty in droplet placement. For during-print part deformation, the disparity between GGF and open-loop can potentially be infinite; in order to determine the efficacy of GGF for correcting during-print part deformations, the particular nature and degree must be considered.

In physical experimentation, the increased geometric fidelity is clear for GGF under uncertainty in assumed layer thickness, valve hold time, substrate shape, and tool pressure (Table II). Additionally, the GGF technique did not require tuning of assumed layer thickness, which turned-out to be a vulnerability of the open-loop method without complete a priori knowledge of the printed components' characteristics.

Of the types of process uncertainties studied in this paper, it is reasonable to presume that traditional closed-loop feedback techniques (as discussed in Section 3) could compensate to some extent for uncertainty in radius of curvature, droplet thickness and possibly droplet placement since these errors occur at the process-variable level. However, none of the techniques would be able to address during-print part deformations, such as those caused by melting, vibration or substrate shift since this occurs at the whole-part geometry level. GGF has an enhanced ability to detect high-level errors and is able to address all of these errors, in addition to others, because it "closes the loop" on a higher level. Instead of monitoring low-level process variables such as temperature or single droplet shape, GGF directly monitors the whole-part geometry.

Another of GGF's advantages stems from the fact that it directly manipulates whole-part geometry. Unlike other techniques that manipulate low-level process variables, GGF directly manipulates overall part shape by iteratively determining locations of droplets. As a result of this direct manipulation, GGF is not reliant on particular models of the relationships between process variables and overall part shape. Also, there is an increased extent to which uncertainties can be handled due to the fact that the geometry is being directly manipulated on a higher, whole-part level. That is, if low-level process variables were being manipulated there is no guarantee that the overall part shape is controllable for all types of process errors (e.g. manipulation of envelope temperature will not necessarily be able to fix errors caused by vibration or evaporation, whereas manipulation of matter placement could).

While this approach has clear advantages in combating sources of uncertainty that operate on the whole-part level, it would require further investigation to determine whether this approach is more effective at handling low-level process uncertainties, as compared to existing feedback control techniques. While the proposed approach has a lesser dependence on modeling the underlying process physics (which is an important advantage), further investigation would still be required to analyze the specific cost/benefit landscape.

While a drop-on-demand approach was used in this paper because it is naturally suited to GGF's iterative decision making, continuous stream material deposition systems could also be used with GGF. However, the material flow would

Table II Summary of RMS surface error for physical experiments

	Open-loop rms surface error (mm) ± standard error ($n = 3$)	RMS surface error normalized to max. part height (%)	Local-GGF RMS surface error (mm) ± standard error ($n = 3$)	RMS surface error normalized to max. part height (%)
No induced process uncertainty (without complete a priori knowledge)	1.98 ± 0.26	40	0.59 ± 0.19	12
No induced process uncertainty (with complete a priori knowledge)	0.58 ± 0.22	12	Not applicable	
Variation in valve hold time	1.33 ± 0.37	27	0.69 ± 0.26	14
Non-flat substrate	1.16 ± 0.24	23	0.36 ± 0.18	7
Reduced deposition tool pressure	2.57 ± 0.83	51	0.34 ± 0.22	7

have to be conceptually discretized; for example, a fused deposition modeling system's polymer stream could be virtually grouped into distinct material packets.

11. Future work

Future work will focus on increasing the complexity of the scoring heuristics to improve GGF performance for specific types of errors. For example, height growth rate terms could be included in the scoring heuristic to give priority to regions of the printed part that are deforming the fastest. Also, surface gradient terms could be included to allow the GGF scheme to prevent the printing of features that are too steep to remain structurally stable.

Additionally, we wish to explore the possibility of creating hybrid control approaches in which the flexibility of GGF is enhanced by usage of some low-level process variable information. While some low-level process variables are related to geometry in very complex manners, other low-level process variables are very well understood. Using knowledge of these stable low-level process variables and their relationships to overall part geometry, perhaps the GGF control scheme could be further improved.

GGF is an approach to implementing robust geometric feedback control in SFF systems. The technique yields benefits over open-loop and existing closed-loop control schemes, for a wide range of process uncertainties. The technique can be specialized for specific types of uncertainties by using more complex scoring heuristics, or GGF can be generalized for implementation in nearly any SFF technique. GGF has the potential to enable SFF to be conducted in unpredictable environments with unreliable materials, and to be applied to novel applications for which the parametric landscape is not easily modeled or controlled.

References

Bodiford, M., Gilley, S., Howard, R., Kennedy, J. and Ray, J. (2005), "Are we there yetdeveloping in situ fabrication and repair (ISFR) technologies to explore and live on the moon and mars", *Proceedings of the AIAA 1st Exploration Conference, Orlando, FL, January 31-February 1, doc. 2624*.

Cohen, D., Malone, E., Lipson, H. and Bonassar, L.J. (2006), "Direct freeform fabrication of seeded hydrogels in arbitrary geometries", *Tissue Engineering*, Vol. 12 No. 5, pp. 1325-35.

Cooper, K., Crocket, R. and Roberts, F. (2004), "Free form fabrication in space", *Proceedings of the 42nd AIAA Aerospace Sciences Meeting and Exhibit Conference, Reno, NV, doc. 1307*.

Derouet, H., Sabatier, L., Coste, F. and Fabbro, R. (1997), "Process control applied to laser surface remelting", *Proceedings of ICALEO, Sec. C*, pp. 85-92.

Doumanidis, C. and Kwak, Y. (2001), "Geometry modeling and control by infrared and laser sensing in thermal manufacturing with material deposition", *Journal of Manufacturing Science and Engineering*, Vol. 123 No. 1, pp. 45-52.

Doumanidis, C. and Skordeli, E. (2000), "Distributed-parameter modeling for geometry control of manufacturing processes with material deposition", *Journal of Dynamic Systems, Measurement, and Control*, Vol. 122, pp. 71-7.

Federovich, N., Alblas, J., Wijn, J., Hennink, W., Verbout, A. and Dhert, W. (2007), "Hydrogels as extracellular matrices for skeletal tissue engineering: state-of-the-art and novel application in organ printing", *Tissue Engineering*, Vol. 13 No. 8, pp. 1905-25.

Hu, D., Mei, H. and Kovacevic, R. (2002), "Improving solid freeform fabrication by laser-based additive manufacturing", *Journal of Engineering Manufacture*, Vol. 216 No. 9, pp. 1253-64.

Lipson, H. (2005), "Homemade: the future of functional rapid prototyping", *IEEE Spectrum*, May, pp. 24-31.

Lovelady, M. and Watts, J. (1999), "Closed-loop feedback for continuous mode materials jetting", *Proceedings of the IEEE/CPMT International Electronics Manufacturing Technology Symposium*, pp. 189-95.

Mallikharjuna, B., Landers, R. and Liou, F. (2001), "Control of laser cladding for rapid prototyping – a review", *Proceedings of the Twelfth Annual Solid Freeform Fabrication Symposium*, pp. 460-7.

Malone, E. and Lipson, H. (2004), "Functional freeform fabrication for physical artificial life", *Proceedings of the Ninth International Conference on the Simulation and Synthesis of Artificial Life*, pp. 100-5.

Malone, E., Rasa, K., Cohen, D., Isaacson, T., Lashley, H. and Lipson, H. (2004), "Freeform fabrication of zinc-air batteries and electromechanical assemblies", *Rapid Prototyping Journal*, Vol. 10 No. 1, pp. 58-69.

Mazumder, J., Schifferer, A. and Choi, J. (1999), "Direct materials deposition: designed macro and microstructure", *Materials Research Innovations*, Vol. 3, pp. 118-31.

Pérès, F. and Noyes, D. (2006), "Envisioning e-logistics developments: making spare parts in situ and on demand", *Computers in Industry*, Vol. 57 No. 6, pp. 490-503.

Sun, L., Jakubenas, K., Crocker, J., Harrison, S., Shaw, L. and Marcus, H. (1998), "*In situ* thermocouples in marco-components fabricatd using SALD and SALDVI techniques", *Materials and Manufacturing Processes*, Vol. 13 No. 6, pp. 909-19.

Taminger, K., Hafley, R. and Dicus, D. (2002), "Solid freeform fabrication: an enabling technology for future space missions", *Proceedings of the 2002 International Conference on Metal Powder Deposition for Rapid Prototyping, Invited Keynote Lecture*.

Vaidyanathan, K. (2000), "Functional metal, ceramic, and composite prototypes by solid freeform fabrication", *JOM Journal of the Minerals, Metals & Materials Society*, Vol. 52 No. 12, p. 30.

Whitney, E. (2004), "Advances in rapid prototyping and manufacturing using laser-based solid free-form fabrication", *The Handbook of Advanced Materials*, Wiley, Oak Ridge, TN, pp. 611-31.

About the authors

Daniel L. Cohen is a PhD candidate in the Department of Mechanical Engineering at Cornell University. He is an National Science Foundation Graduate Research Fellow and a US Department of Homeland Security Graduate Fellow. His research interests are in tissue engineering SFF, *in situ* SFF and closed-loop geometric feedback control of SFF systems. Daniel L. Cohen is the corresponding author and can be contacted at: dlc44@cornell.edu

Hod Lipson is an Assistant Professor at Cornell University in the Department of Mechanical Engineering, as well as in Computing and Information Science. He leads the Computational Synthesis Laboratory. Professor Lipson holds a PhD from the Technion. His research interests are in functional SFF and evolutionary robotics.

To purchase reprints of this article please e-mail: **reprints@emeraldinsight.com**
Or visit our web site for further details: **www.emeraldinsight.com/reprints**